Materials Science & Engineering A 865 (2023) 144611

Contents lists available at ScienceDirect

Materials Science & Engineering A

journal homepage: www.elsevier.com/locate/msea

Microstructures and mechanical behavior of non-equiatomic $Co_{29}Cr_{29}Fe_{29}Ni_{13\text{-}x}V_x$ high-entropy alloys at room and cryogenic temperatures

Chengbin Wei [a,b], Yiping Lu [a,c,*], Tongmin Wang [a,c,**], Peter K. Liaw [d]

[a] *Key Laboratory of Solidification Control and Digital Preparation Technology (Liaoning Province), School of Materials Science and Engineering, Dalian University of Technology, Dalian, 116024, China*
[b] *College of Electromechanical Engineering, Qingdao University of Science & Technology, Qingdao, 266061, China*
[c] *Engineering Research Center of High Entropy Alloy Materials (Liaoning Province), School of Materials Science and Engineering, Dalian University of Technology, Dalian, 116024, China*
[d] *Department of Materials Science and Engineering, The University of Tennessee, Knoxville, TN37996, USA*

ARTICLE INFO

Keywords:
High-entropy alloys
Microstructure
Dislocation
Mechanical properties
Strain hardening

ABSTRACT

A series of non-equiatomic $Co_{29}Cr_{29}Fe_{29}Ni_{13\text{-}x}V_x$ (x = 0, 0.5, 3, and 5) high-entropy alloys (HEAs) with fully recrystallized microstructures were prepared by rolling and annealing. The microstructures were characterized and the mechanical properties were obtained at different temperatures. The recrystallization and grain-growth behavior of the alloys are retarded owing to the addition of V. The lattice friction stress increases drastically with the addition of a minor of V. Ultrahigh yield strengths of 1.8 GPa and 1.4 GPa, and considerable tensile ductility values of ~30% and ~50% were developed at a cryogenic temperature (77 K) for the 700 °C-annealed and 800 °C-annealed alloys. The strengthening mechanism and deformation behavior at cryogenic temperatures were investigated. The comprehensive mechanical properties of the alloy at low temperatures are better than those of most reported HEAs. The alloy is easy to process and prepare and therefore, has considerable potential for industrial applications.

1. Introduction

High-entropy alloys (HEAs) tend to form single-phase structures, such as the face-centered-cubic (FCC), body-centered-cubic (BCC), or hexagonal close-packed (HCP) phase. Consequently, many HEAs possess excellent properties that cannot be obtained by conventional materials, such as outstanding cryogenic mechanical properties [1], high strength [2–4], good corrosion and wear resistance [5,6], and superior high temperature performance and thermal stability [7–9].

Among various HEAs, the ones with an FCC structure attracts considerable attention because of their potential ductility over a wide temperature range from cryogenic to elevated temperatures. The quinary CoCrFeMnNi alloy was one of the first equiatomic HEAs to be characterized as an FCC solid solution, and it has been widely investigated with respect to its mechanical properties, deformation mechanisms, fracture toughness, etc. [1,9–11]. However, the low yield strength of these FCC-structured HEAs makes it unsuitable for industrial applications. Many methods have been adopted to overcome these shortcomings and increase the yield strength (YS) of the FCC-structured HEAs. Except for precipitation, heterogeneous structure, grain refinement, and severe plastic deformation (SPD) [12–16], an effective approach is to remove or replace elements from the CoCrFeMnNi alloy to reduce the stacking fault energy (SFE) and realize the twinning induced plasticity (TWIP) and transformation induced plasticity (TRIP) effects, and thus, achieve the superior mechanical properties [17–20].

In addition, solid-solution hardening also plays an important role in improving the strengths of HEAs. The lattice distortion hinders the dislocation slip and contributes to solid-solution hardening [21–23]. Sohn et al. [24] designed a novel VCoNi medium-entropy alloy (MEA) with high yield strength, which contributes to the high-level lattice

---

* Corresponding author. Key Laboratory of Solidification Control and Digital Preparation Technology (Liaoning Province), School of Materials Science and Engineering, Dalian University of Technology, Dalian, 116024, China.
** Corresponding author. Key Laboratory of Solidification Control and Digital Preparation Technology (Liaoning Province), School of Materials Science and Engineering, Dalian University of Technology, Dalian, 116024, China.
E-mail addresses: luyiping@dlut.edu.cn (Y. Lu), tmwang@dlut.edu.cn (T. Wang).

https://doi.org/10.1016/j.msea.2023.144611
Received 11 November 2022; Received in revised form 5 January 2023; Accepted 7 January 2023

Table 1
Anneal temperatures used on different alloys.

Alloys	V0	V0.5	V3	V5
Annealing temperatures (°C)	675, 700, 800, 900	675, 700, 800, 900	675, 800, 900, 1000, 1200	800, 900, 1000, 1200

distortion. Compared to CoCrNi, CoCrNiW$_x$ alloys exhibited the high lattice friction stress and strength [25]. Thus, large atoms that enhance the lattice distortion and the mechanical properties are introduced into the matrix. In addition, the SFE can also be changed by modifying the lattice distortion, which is an important factor that affects the mechanical properties and deformation mechanisms of FCC-structured HEAs [26,27]. A pioneering study [28] indicated that the SFE could be tailored to a wide range of values by altering the composition and the low-Ni alloys had a much lower SFE compared with the equiatomic CoCrFeNi alloy system. In the system of Co–Cr–Fe–Ni alloys, the SFE of the Ni element was the highest. The SFE of Ni-based superalloy was systematically decreased with the addition of Co and Cr, while the addition of Fe failed to change the SFE of Ni-based superalloy significantly [29,30]. The addition of other elements, such as V element, to Ni-based alloys could also decrease the SFE of the alloys [31]. Adding an element with a large radius is an important means to improve the yield strength of FCC-phase HEAs via solid solution strengthening. The radius of V element is larger than Co, Cr, Fe, and Ni element. Hence, the V element was chosen for adding into the Co–Cr–Fe–Ni HEA system in this study. It is reported that the mechanical properties of the HEAs can be improved by the addition of elements like Al [32], Ti [33], Nb [34], Mo [35]. However, the alloy will be produce biphasic or multiphasic structures with increasing the alloying elements [33–35]. In order to obtained the single FCC phase alloy, small amount of V element was added in this study.

Based on the above discussion, a series of $Co_{29}Cr_{29}Fe_{29}Ni_{13\text{-}x}V_x$ (x = 0, 0.5, 3, and 5, at. %) alloys were designed and prepared. The effects of V on the microstructures and mechanical properties of the alloys were also studied.

2. Experimental methods

Alloys with a nominal composition of $Co_{29}Cr_{29}Fe_{29}Ni_{13\text{-}x}V_x$ (x = 0, 0.5, 3, 5, denoted as V0, V0.5, V3, and V5 alloys, respectively) were prepared, using a compact vacuum-induction melting equipment in an argon atmosphere. The raw materials were high-purity (>99.95% wt.) Co, Cr, Fe, Ni, and V metal particles. Approximately 110 g of the master alloy was melted and poured into a rectangular module. To ensure a chemical homogeneity, majority of the ingots were homogenized at 1200 °C for 2 h. And then they were multipass hot-rolled at 900 °C with a reduction ratio of 30%. Following this process, the sheets were homogenized at 1200 °C for 2 h, followed by water quenching. The purpose of this homogenization treatment is to eliminate the precipitation produced during the hot rolling process and obtain a single FCC structure with fully recrystallized microstructure. And these processes could also be ensured the alloys without defects before cold tolling. Subsequently, the sheets were rolled to 2 mm at room temperature (RT, 25 °C) as the final sheets.

The tensile samples were cut from the as-cast ingots and rolled sheets

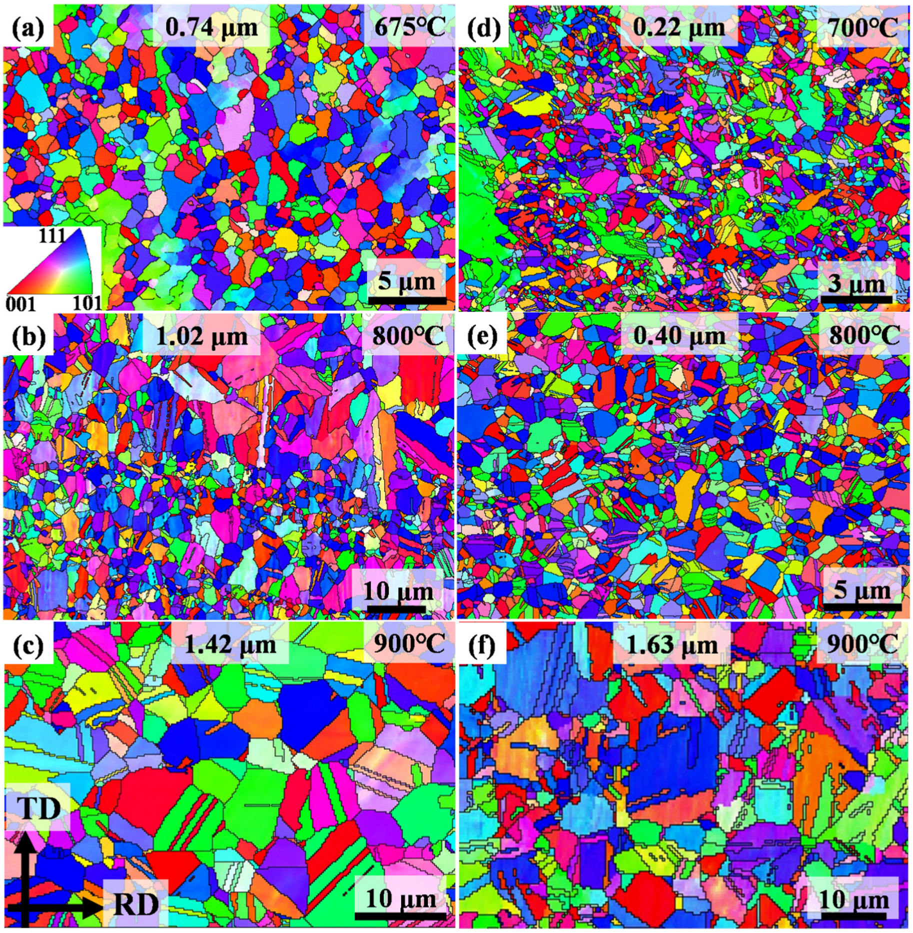

Fig. 1. EBSD IPF maps of V0 alloy after rolling and annealing at (a) 675 °C, (b) 800 °C, and (c) 900 °C for 1 h and V0.5 alloy after annealing at (d) 700 °C, (e) 800 °C, and (f) 900 °C for 1 h.

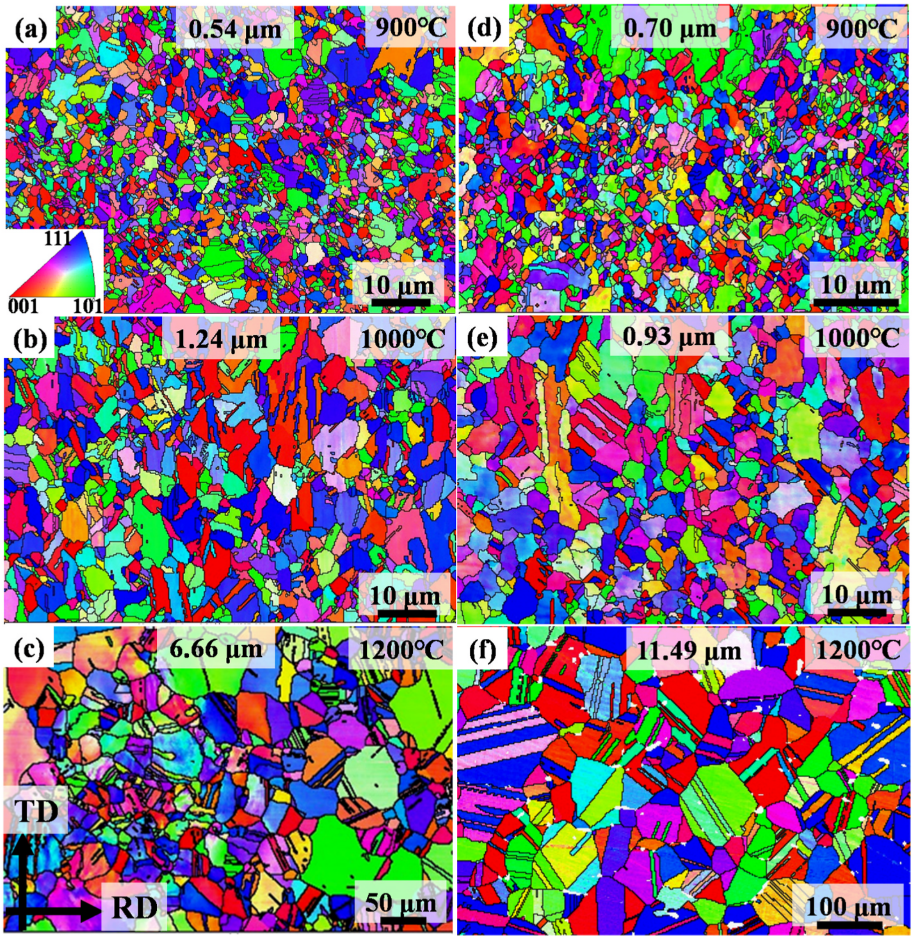

Fig. 2. EBSD IPF maps of the V3 alloy after rolling and annealing at (a) 900 °C, (b) 1000 °C, and (c) 1200 °C for 1 h and V5 alloy at (d) 900 °C, (e) 1000 °C, and (f) 1200 °C for 1 h.

along the height of the ingot and rolling direction (RD), respectively. The RT tensile tests were performed, using a machined dog-bone-shaped sample with a gauge length of 12.5 mm and width of 3 mm. In order to statistic the grain size and investigate the grain growth behavior, the alloy with fully recrystallized were chosen in our study. Hence, different temperature parameters were used on different alloys. The annealing temperature were ranged from 675 °C to 1200 °C and quenched with water. The detail of the anneal temperatures were summarized in Table 1. All tests were carried out, using an Instron 5569 machine with a strain rate of 10^{-3} s^{-1} at RT.

For the 77 K experiments, flat dog-bone tensile specimens with a gauge length of 25 mm and width of 4 mm were used. The tensile specimens and grip were completely immersed in liquid nitrogen for 15 min Before the tensile test. To ensure that the tensile specimens are held at a target temperature, they are always submerged in liquid nitrogen during tensile testing. Tensile tests were carried out, employing an Instron 5582 machine with a strain of 10^{-3} s^{-1}.

Microstructures of the alloy in the as-rolled and other conditions were analyzed, using different methods. X-ray diffraction (XRD) measurements were performed, employing an Empyrean machine equipped with Cu K-α radiation operated at 40 KV and 30 mA between 30° and 100° (2θ) with a step size of 6°/min. The tensile fracture morphologies were observed, using SUPARR 55 scanning electron microscope (SEM). Electron backscatter diffraction (EBSD) measurements were carried out by a Helios G4UX SEM, and the data were analyzed, using a Channel 5 software. The samples for EBSD measurements were first mechanically and then electrically polished in a solution of perchloric acid (10%, volume percent) and ethanol (90%, volume percent) at a voltage of 15 V. The chemical compositions and elemental mappings of the samples were studied via a JXA-8530F PLUS electron probe microscope (EPMA).

Transmission electron microscopy (TEM) characterization was conducted, using a JEOL 2100F machine operated at 200 kV. The specimens for TEM investigations were prepared by mechanical polishing, followed by twin-jet electro-polishing (electrolyte: 93% ethanol + 7% perchloric acid volumetrically) with a potential of 25 V.

3. Results

3.1. Microstructures during annealing

The EBSD inverse pole figure (IPF) maps of V0, V0.5, V3, and V5 alloys after rolling and annealing at different temperatures are shown in Figs. 1 and 2. For the V0 alloy, the microstructure consists of nearly-complete recrystallized grains with a mean size of ~0.74 µm after annealing at 675 °C, as shown in Fig. 1 (a). With the increase in the annealing temperature, the partial grains grow and a heterogeneous structure with a mean grain size of ~1.02 µm is developed at 800 °C, as presented in Fig. 1 (b). After annealing at 900 °C, the grains grow to ~1.42 µm. Different from the V0 alloy, the grain size is only about ~0.22 µm after annealing at 700 °C for the V0.5 alloy. The grain size changes slightly when the annealing temperature reaches 800 °C, and it is smaller than that of the V0 alloy (See Fig. 1 (e)). At an annealing temperature of 900 °C, the coarse grains are formed with a mean size of ~1.63 µm, which is larger than that of the V0 alloy (See Fig. 1 (f)). For the V3 and V5 alloys, the completely-recrystallized grains are observed at 900 °C for 1 h. With increasing the annealing temperatures from

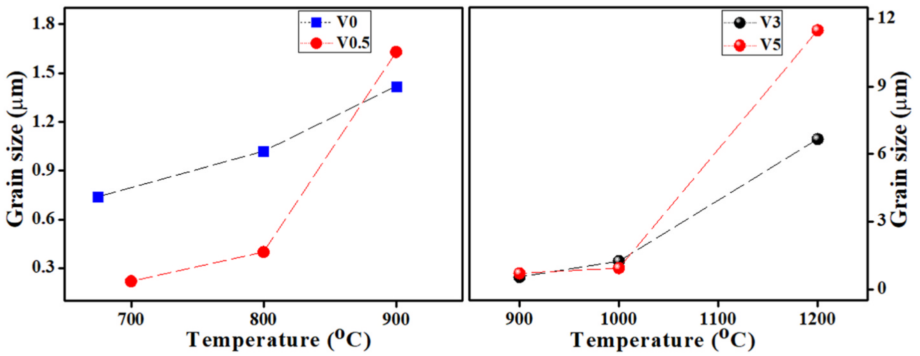

Fig. 3. Mean grain sizes of alloys as a function of the annealing temperature.

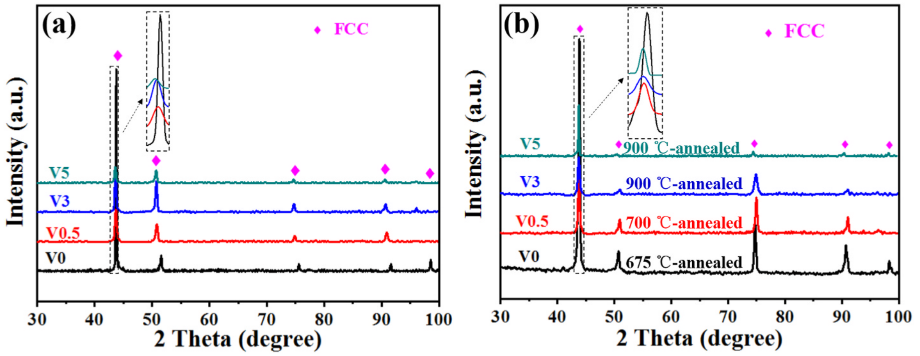

Fig. 4. XRD patterns of the V0, V0.5, V3, and V5 alloys: (a) After homogenization at 1200 °C; (b) After annealing at different temperatures. The annealing temperatures for V0 and V0.5 are 675 °C and 700 °C, respectively. The annealing temperature for both V3 and V5 is 900 °C.

Table 2
Chemical compositions (at. %) of the fully-recrystallized alloys.

Alloys		Co	Cr	Fe	Ni	V
V0	Nominal	29	29	29	13	0
	Experimental	28.84	29.28	28.91	12.97	0
V0.5	Nominal	29	29	29	12.5	0.5
	Experimental	28.52	29.46	29.54	11.96	0.52
V3	Nominal	29	29	29	10	3
	Experimental	28.31	30.32	28.90	9.50	2.97
V5	Nominal	29	29	29	8	5
	Experimental	28.49	29.87	28.89	7.78	4.97

900 °C to 1200 °C, the grains grow from 0.54 μm to 6.66 μm for the V3 alloy (Fig. 2(a–c)). For the V5 alloy, the grains grow more rapidly as the annealing temperature increases. With the increase in the annealing temperature, the mean grain size changes from 0.70 μm to 11.49 μm. The results of these grain sizes are plotted in Fig. 3.

The XRD patterns of these alloys after homogenization and annealing reveal a single FCC structure, as presented in Fig. 4(a and b). But the peaks were shifted slightly with an increasing of V element. These structures can be verified by the local magnification of the XRD patterns, as shown in the inserts of Fig. 4 (a) and (b). These phenomena were resulted from the solid solution of V element. Chemical compositions of the fully-recrystallized alloys are listed in Table 2. Partial EPMA results were chosen in present study to further explain the microstructure of the alloys. And the EPMA maps of the 675 °C-annealed V0 alloy and 900 °C-annealed V5 alloy are shown in Fig. 5. It indicates that all the elements are uniformly distributed in the V0 and V5 alloy. And these results are consistent with the XRD results, which revealed only a single-phase structure, as shown in Fig. 4 (b).

3.2. Mechanical properties under tensile deformation at room temperature

Fig. 6 (a) shows the RT tensile engineering strain-stress curves of the V0 alloy. The as-cast V0 alloy had a YS, ultimate tensile strength (UTS), and fracture elongation (EL) of 327 MPa, 617 MPa, and 25%, respectively. After two-stage rolling, the strength increased by four times to 1670 MPa. But there is a sharp deterioration in plasticity, and it fractured immediately after yield. In this case, grain-boundary strengthening and dislocation strengthening are considered to be the primary strengthening mechanisms.

As in the case of conventional alloys, the enhancement in ductility after annealing was achieved at the expense of strength, and the YS of the V0 alloy reached to 1.3 GPa after annealing at 675 °C. And the total elongation is 13%. Meanwhile, the flow stress reaches its peak value and then softens with the strain increased. This phenomenon often occurs when an annealed specimen is deformed by rolling [36]. Due to the grain growth and dislocation density decrease, annealing-induced softening was commonly observed in alloys. Annealing-induced hardening was also observed earlier, which was caused by precipitation hardening, nano-twin formation and grain-boundary relaxation [37,38]. In the present work, annealing-induced hardening may be attributed to grain-boundary relaxation, which is similar for the CoCrFeMnNi and the CoCrNi alloy [38,39]. The EL increased to 40% as the annealing temperature rose to 700 °C. In general, the annealing process increases the hardening ability and is characterized by a strain-hardening stage in the tensile test. The V0.5, V3, and V5 alloys exhibited mechanical properties similar to the V0 alloy after annealing at different temperatures. For all the $Co_{29}Cr_{29}Fe_{29}Ni_{13\text{-}x}V_x$ alloys, the EL increased, and the strength decreased with the increase in the annealing temperature. Fig. 7 shows the mechanical properties of the V*x* alloys after annealing at 800 °C. The YS and UTS of the V5 alloy are 1320 MPa and 1500 MPa, respectively. Meanwhile, the EL decreased sharply from 53.5% for the V0 alloy to

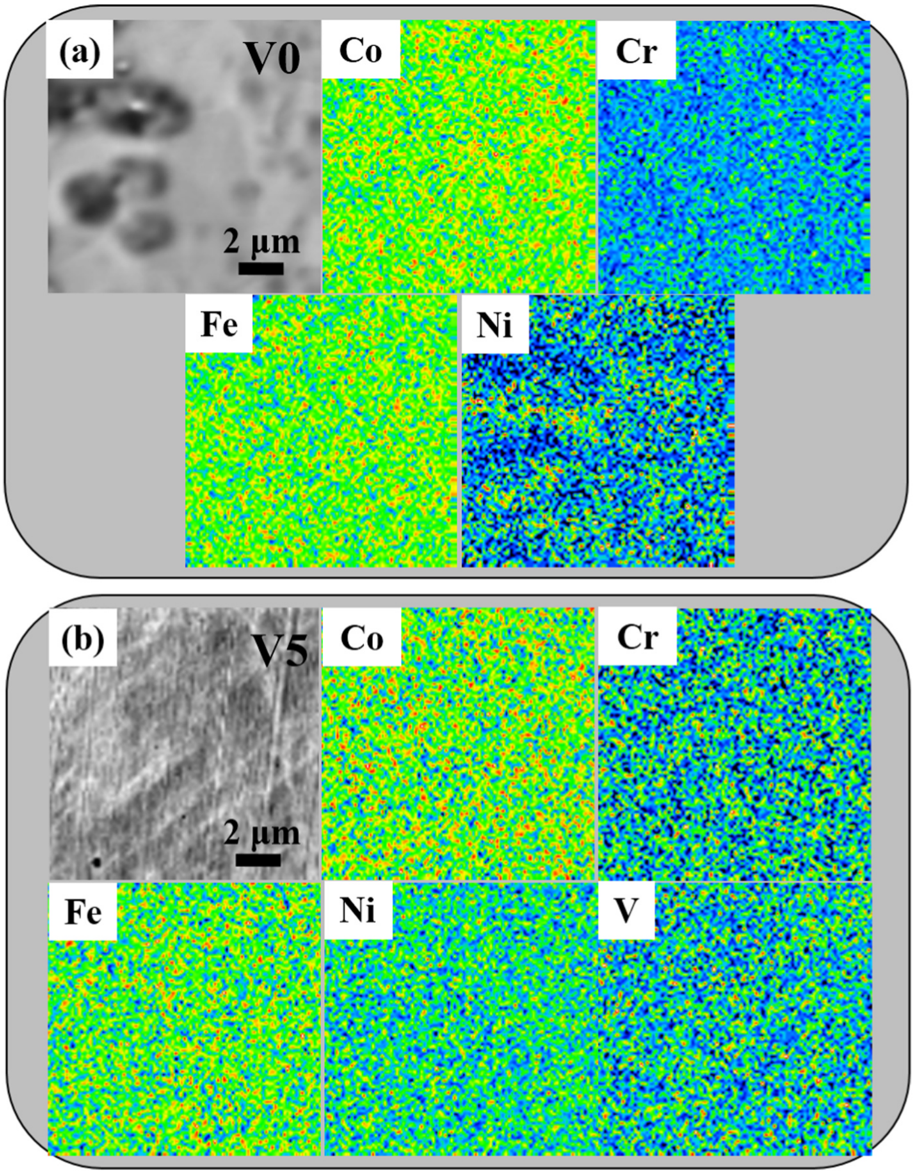

Fig. 5. EPMA maps of the V0 alloy after annealing at 675 °C (a) and V5 alloy after annealing at 900 °C (b).

6.6% for the V5 alloy. For the V5 alloy annealed at 800 °C, the poor ductility may result from the deformation microstructure and high density of dislocations. With the increase in the anne1aling temperature, recrystallization and grain growth occur, and the ductility increased as the strength decreased.

3.3. *Cryogenic properties and strain-hardening behavior of the V0.5 alloy*

In order to explain the excellent mechanical properties and deformation mechanisms, the alloy with remarkable combination of strength and tensile ductility at 77 K were selected in present study. Fig. 8(a and b) show the mechanical properties of the 700 °C-annealed and 800 °C-annealed V0.5 alloys at RT and 77 K. The figure indicates an exceptional strength-ductility combination and superior YS and UTS values of ~1.8 GPa and ~1.84 GPa for the 700 °C-annealed alloy when compared to ~1.4 GPa and ~1.7 GPa for the 800 °C-annealed alloy at 77 K, respectively. The elongation also retained ~30% for the 700 °C-annealed alloy and ~50% for the 800 °C-annealed alloy, respectively. The excellent mechanical properties may be attributed to the high strain hardening rate of the V0.5 alloy. The strain-hardening-rate curve superimposed with the true stress curve of the 700 °C- and 800 °C-annealed alloy is shown in Fig. 8 (b). For 800 °C-annealed alloy, the strain-hardening-rate curve is characterized by four regions. In Region I, the strain-hardening rate dropped sharply to 2.4 GPa, which is associated with the elastic to plastic transition. In Region II, the strain-hardening rate increases rapidly and then drops gradually. In Region III, the strain-hardening rate increases again and reaches a peak value of 3.4 GPa. With further increase in the strain, the strain-hardening rate remains constant initially and then decreases progressively, which is already in Region IV.

The increase of the strain-hardening rate in Region III and the persistent high value in a certain range of Region IV is unique during the tensile process. This high-strain-hardening rate was rarely reported among the single FCC phase HEAs deformed at cryogenic temperatures [10,40,41]. It is worth noting that the fracture surface has two regions corresponding to the 700 °C-annealed and 800 °C-annealed alloys. The central flat fracture region and the peripheral shear-lip region are marked with the black dashed line in Fig. 9 (a) and (d). Both regions of the 700 °C-annealed and 800 °C-annealed alloys have numerous dimples that indicate a characteristic mode of ductile fracture at 77 K, as presented in Fig. 9 (b), (c), (e), and (f). The depth of the dimples at the center is larger than that of the shear lip region.

A comparison of the YS of these alloys with published values for

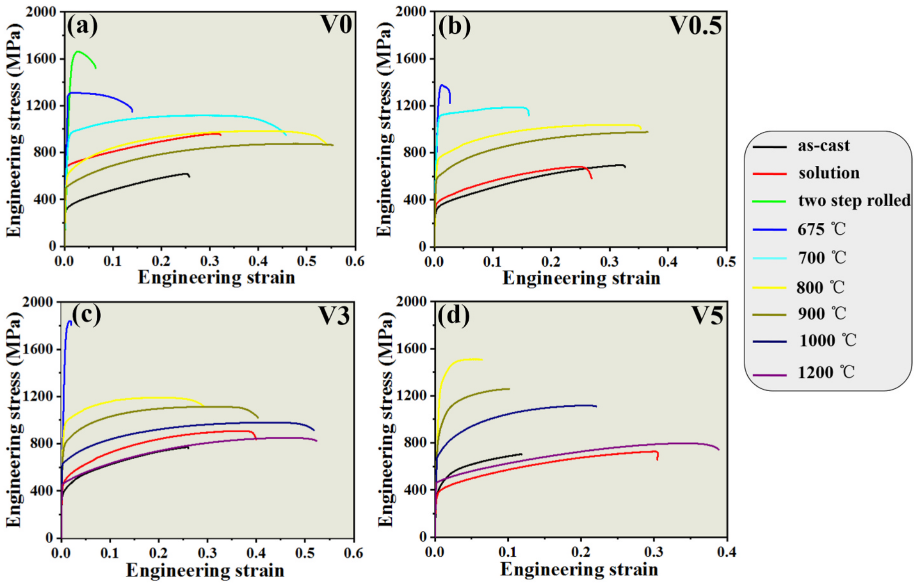

Fig. 6. Room-temperature engineering tensile strain-stress curves of the (a) V0, (b) V0.5, (c) V3, and (d) V5 alloys after annealing at different temperatures.

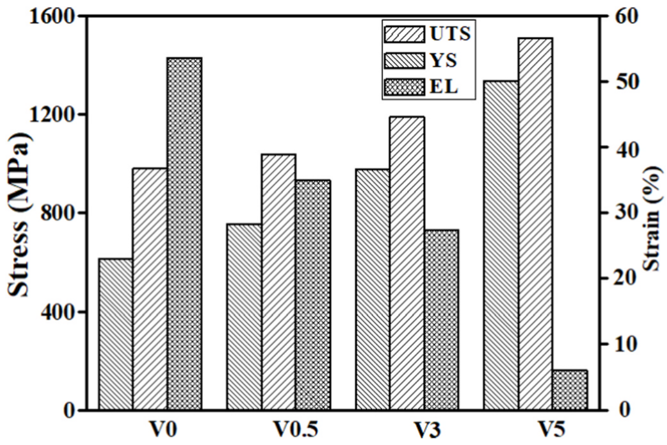

Fig. 7. Room-temperature mechanical properties of these alloys after annealing at 800 °C.

HEAs and conventional alloys is exhibited in Fig. 10. The outstanding cryogenic mechanical properties are particularly noteworthy, and surpass those of the existing HEAs/MEAs, including AISI 304 stainless steel and high-Mn steel [1,2,10,11,40–51].

4. Discussion

4.1. Grain growth

The grain growth, which will be taken specifically to refer to the increase in the grain size that results from annealing after recrystallization, occurred by the migration of grain boundaries. The kinetics of grain growth are described by the following equation [52,53]:

$$D_f^n - D_0^n = Ct \tag{1}$$

where D_0 is the initial grain size, D_f is the measured mean grain size, t is the annealing time, n is the kinetic coefficient quantifying the grain-growth behavior, and C is the constant related to the mobility and surface energy of the grain boundary that depends on the temperature, T, according to the following equation [54]:

$$C = C_0 \exp(-Q/RT) \tag{2}$$

where C_0 and R are, respectively, an arbitrary constant and the gas constant, and Q is the activation energy for grain boundary migration.

In the classical grain-growth theory, the value of n is typically in the range of 2–4 [55]. Before annealing at different temperatures, the alloys experience severe mechanical deformation, and D_0 is small enough to be neglected [56]. Hence, the Q value can be calculated from the plot of $\ln\{(D_f^n - D_0^n)/t\}$ against the reciprocal of the annealing temperature, as shown in Fig. 11. Based on the slopes of the dashed lines in Fig. 11, the Q

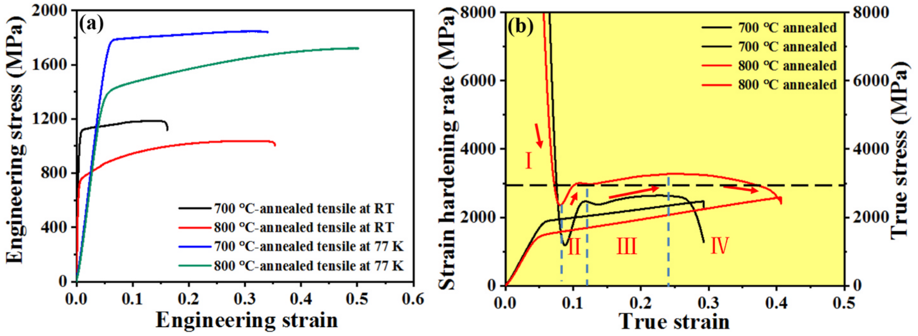

Fig. 8. (a) Engineering tensile curve of the V0.5 alloy at RT and 77 K after annealing at 700 °C and 800 °C. (b) Strain-hardening rate and true stress as a function of true strain for the 700 °C- and 800 °C-annealed alloy.

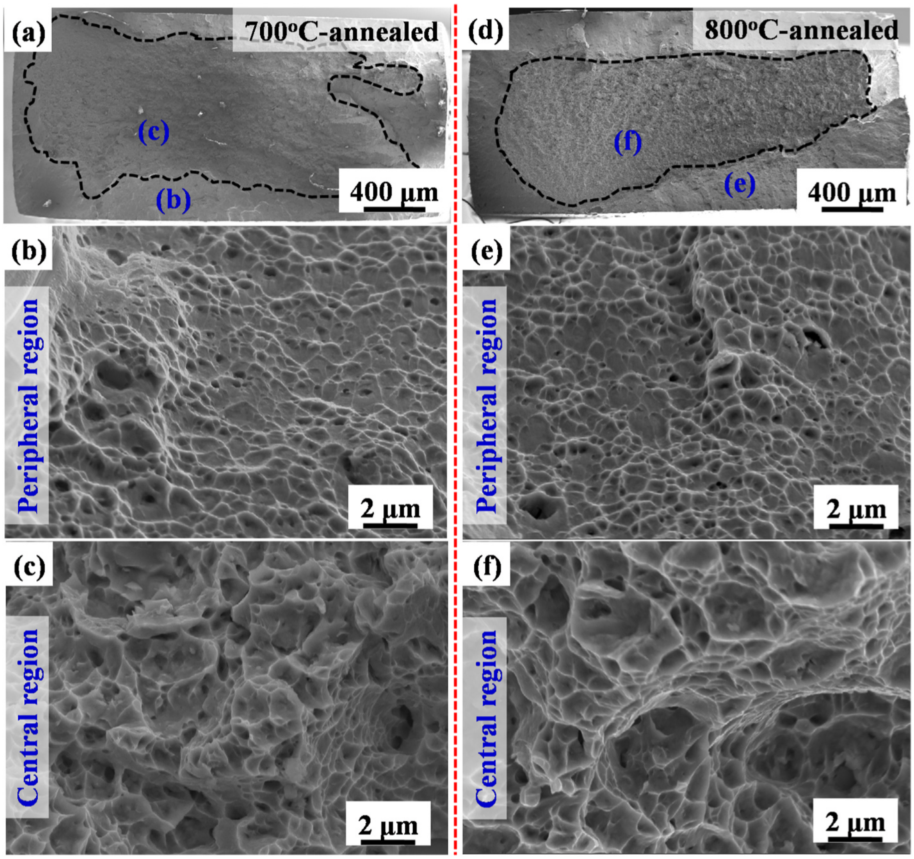

Fig. 9. Fracture surface deformed at 77 K of (a) 700 °C-annealed alloy and (d) 800 °C-annealed alloy. High-magnification fracture surface of the peripheral shear-lip region (b) and central flat fracture region (c) for the 700 °C-annealed alloy. High-magnification fracture surface of the peripheral shear-lip region (e) and central flat fracture region (f) for the 800 °C-annealed alloy.

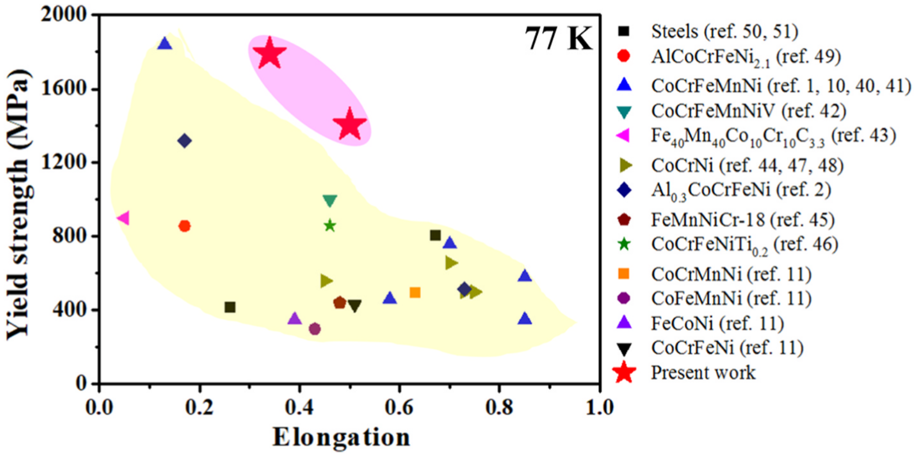

Fig. 10. Comparison of YS and EL of the investigated alloy with other reported classic HEAs and conventional alloys [1,2,10,11,40–51].

values of the V3 alloy are higher than that of the V0 alloy for the same n values. First, the addition of V produced the solute-drag effect, resulting in the slow grain-coarsening kinetics. And second, the increase in Q at high temperatures in the V3 alloy documents its high efficiency in hampering the grain-coarsening kinetics. The high value of the index, n, indicates the slow grain coarsening kinetics.

These results indicate that the difference in grain sizes among these alloys is a result of the content of the V element. The formation of precipitates will exert a retarding force or pressure on the grain boundary, which may influence the recrystallization and grain growth [57]. Besides, V has a larger atomic radius than Co, Cr, Fe, and Ni, which improves the retarding effects during recrystallization and grain growth [25]. Similar phenomena have been observed in previous works [25, 27]. The details of retarding effects on the recrystallization by the addition of V need further investigation.

4.2. Strengthening mechanisms at room temperature and 77 K

The enhancement of YS due to the addition of V is significant. The strengthening mechanisms of polycrystalline alloys include solid-

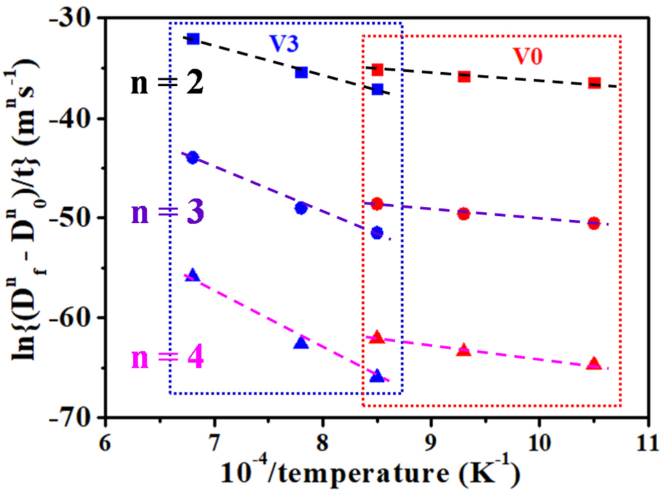

Fig. 11. Activation energy of grain growth for the V0 (red dashed box) and V3 (blue dashed box) alloys. The *n* values were 2 (black dashed line), 3 (purple dashed line), and 4 (pink dashed line), respectively. (For interpretation of the references to colour in this figure legend, the reader is referred to the Web version of this article.)

Table 3
Grain size, yield strength (YS), and the calculated value of these alloys.

Alloys	Grain size (μm)	YS (MPa)	k (MPa·μm$^{0.5}$)	σ_0 (MPa)
V0	1.09	540	367.9	188
	1.77	465		
	2.97	401		
V0.5	0.40	755	264.9	336
	0.89	617		
	1.63	545		
V3	0.54	760	296.4	356
	1.24	625		
	6.66	470		
V5	0.70	751	318.2	366
	0.93	690		
	11.49	461		

solution strengthening (σ_s), grain-boundary strengthening (σ_g), dislocation strengthening (σ_d), and precipitation strengthening (σ_p). For fully-recrystallized alloys in present study, the contribution of σ_d and σ_p may be neglected. Hence, the strengthening mechanisms in these alloys are mainly solid-solution strengthening and grain boundary strengthening.

Grain-boundary strengthening can be represented by the Hall-Petch equation [12]:

$$\sigma_g = \sigma_0 + kd^{-0.5} \tag{3}$$

where σ_0 is the lattice friction stress, k is the Hall-Petch slope, and d is the average grain size. The k values of Vx alloys are not reported in the literature. Hence, σ_0 and k of Vx alloys need to be calculated, based on the experimental results [25,58]. The calculated k of V0, V0.5, V3, and V5 alloys are 367.9 MPa μm$^{0.5}$, 264.9 MPa μm$^{0.5}$, 296.4 MPa μm$^{0.5}$, and 318.2 MPa μm$^{0.5}$, respectively. The calculated σ_0 of V0, V0.5, V3, and V5 alloy are 188 MPa, 336 MPa, 356 MPa, and 366 MPa, respectively. The calculated value of these alloys at different grain sizes are listed in Table 3. The results are different from the values reported for CoCrFeMnNi alloy [10] and other medium-entropy alloys [24,47,58]. The difference is closely related to the alloying element. The crystal lattices of the alloys are distorted result from the addition of large atomic sizes V element, and the reason for the high lattice friction stress is due to the lattice distortion effect [58].

Solid-solution strengthening in HEAs are related to the lattice stress [11]. In the present study, the increase in YS can be described as the difference of σ_0 between the Vx alloys (x = 0.5, 3, and 5) and the reference V0 alloy. Based on the calculated σ_0 values, the increment in YS due to the solid solution strengthening for the V0.5 alloy is 148 MPa, while the increments for V3 and V5 are 168 MPa and 178 MPa, respectively. This trend indicates that solid-solution strengthening increases significantly due to the addition of a minor quantity of V. The lattice-friction stress also increased with the addition of V. Sohn's [24] research indicated that the addition of V can introduce large fluctuations of atomic-bond distances, eventually resulting in the increased lattice distortion and friction stress [59]. In present study, the lattice parameter was 3.5501 Å,3.5602 Å, 3.5729 Å, and 3.5843 Å for V0, V0.5, V3, and V5 alloy, respectively. V has a larger atomic size than Co, Cr Fe and Ni, and the larger atomic size differences can generate higher friction stresses when dislocations pass through the alloy.

Similarly, the solid-solution strengthening and grain-boundary strengthening are the main strengthening mechanisms for the high YS at cryogenic temperatures, and the YS can be expressed by the following equation:

$$\sigma_{YS}(T) = \sigma_s + \sigma_g \tag{4}$$

where σ_{YS} is the YS, and σ_s is the contribution from the solid solution.

According to Cordero et al. [60], the Hall-Petch slope can be written as below:

$$k = \beta G b^{0.5} \tag{5}$$

where β is a constant, b is the Burgers vector, and G is the shear modulus, respectively. According to the Hall-Petch relationship, on combining Equations (3) and (5), Equation (4) becomes:

$$\sigma_{YS} = \sigma_s + \Delta\sigma_{0(T)} + \Delta G_{(T)}\beta b^{0.5} d^{-0.5} \tag{6}$$

The shear modulus, G, is slightly temperature-dependent [61]. Solid solution-strengthening can be incorporated into the σ_0 [11]. Hence, Equation (6) can be written as:

$$\sigma_{YS} \propto \sigma_{0(T)} \tag{7}$$

The dislocation line energy in HEAs is a variable, in contrast to conventional FCC alloys [62,63]. This fluctuation will affect the dislocation mobility to overcome the lattice-friction stress. The Peierls-Nabarro (P–N) stress, $\sigma_{P\text{-}N}$, which is controlled by the influence of temperature on the width of the dislocations, dominated the lattice friction. The value of $\sigma_{P\text{-}N}$ could be calculated as the following Equation [11]:

$$\sigma_{P-N} = \frac{2G}{1-\vartheta}\exp\left(\frac{-2\pi\omega_0}{b}\right) * \exp\left(\frac{-2\pi\omega_0}{b}\right)\alpha T \tag{8}$$

where ϑ is the Poisson's ratio, ω_0 is the dislocation width at 0 K, α is a positive constant, and T is the test temperature, respectively. It suggests that the P–N stress would be exponentially amplified by the temperature.

4.3. Deformation mechanisms at 77 K

To understand the exceptional mechanical properties of the alloys at 77 K, the microstructure of the 800 °C-annealed V0.5 alloy after tensile deformation at 77 K was investigated by TEM. It can be observed that deformation occurs by the dislocations and stacking faults (SFs), as shown in Fig. 12 (a), marked with white ellipses. Dislocations are localized at the grain and twin boundary, as marked with white arrows in Fig. 12 (a). The deformation structures were also detected in the annealing twins to further synergize the deformation of the alloy. Also, some SF bundles are formed in the alloy during the deformation process, as shown in the high-resolution TEM image of Fig. 12 (b), which is marked with red arrows. There are also some dislocations in the SFs free

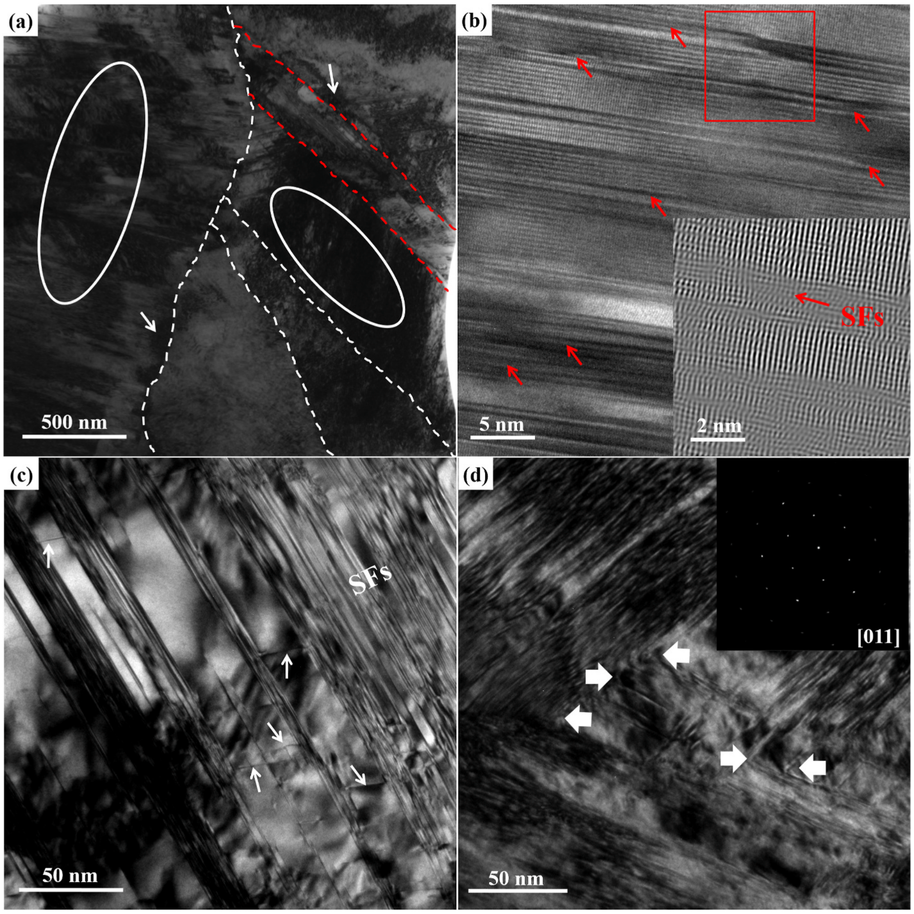

Fig. 12. (a) Bright-field TEM microstructure of the V0.5 alloy after tensile at 77 K. The grain boundaries are highlighted by white dashed lines and twin boundaries represented by red dashed lines. (b) High-resolution TEM image of SFs. The insert shows the magnified inverse fast Fourier transform image showing the SFs marked by a red square in (b). The images, (c) and (d), are the bright-field TEM images of dislocations, SFs and L-C locks. (For interpretation of the references to colour in this figure legend, the reader is referred to the Web version of this article.)

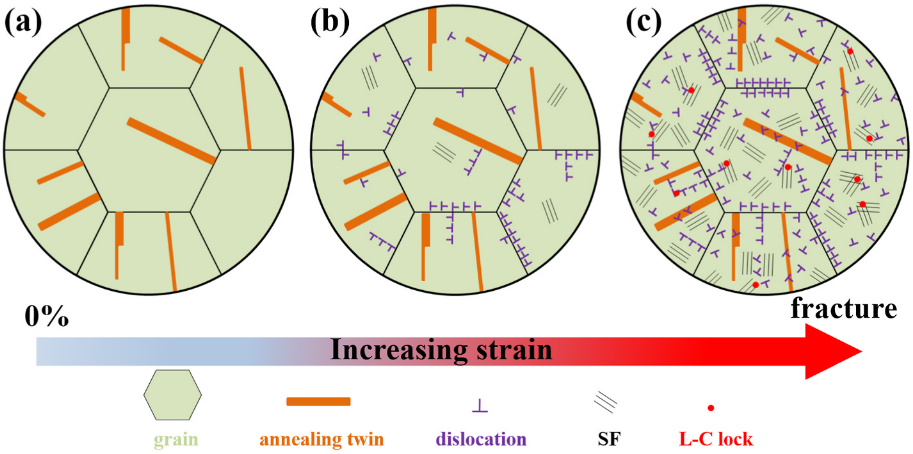

Fig. 13. Schematic sketches illustrating the microstructure evolution and deformation mechanisms in the 800 °C-annealed V0.5 alloy during tensile deformation at 77 K: (a) recrystallized microstructure; (b) initial deformation stage; (c) fracture.

regions, as shown in Fig. 12 (c). The high-density SFs can pin the motion of dislocations by decreasing their mean free path and enhancing the strain hardening of the alloy [40]. In addition, the Lomer-Cottrell (L-C) locks, which result from the interaction of two partial dislocations, as shown in Fig. 12 (d), act as obstacles that effectively pin the motion of dislocations and further enhance strain hardening [64]. The L-C locks can also be served as Frank-Read sources for dislocation multiplications that lead to strain hardening [65]. Meanwhile, the density of the SF and L-C locks increase as plastic deformation proceeds, and their strain-hardening effects are enhanced [66,67]. The recrystallized microstructure and lattice friction lead to stable mechanical properties of the V0.5 alloy at 77 K. Consequently, the V0.5 alloy exhibits both excellent ductility and high strength.

Schematic sketches for the deformation mechanisms and the feature of deformed microstructure in the 800 °C-annealed V0.5 alloy at 77 K is shown in Fig. 13. After annealed at 800 °C, the V0.5 alloy was exhibited fully recrystallized microstructure and lots of annealing twins were observed in the recrystallized microstructure (Fig. 1e). And the annealing twins were indicated by orange line in the schematic sketches as shown in Fig. 13 (a). At the early stage, deformation initiates by dislocation slip and SFs, and then is their interaction dominated the deformation with increasing the plastic strain. The number of dislocation and SF were also increased with increasing the strain and accumulated at grain and twin boundaries, as shown in Fig. 13 (b) and (c). All of the dislocations and SFs were played a major role in the increased strength, ductility, and strain hardening capacity of the V0.5 alloy at 77 K.

5. Conclusions

A series of $Co_{29}Cr_{29}Fe_{29}Ni_{13-x}V_x$ ($x = 0$, 0.5, 3, and 5, at. %) HEAs were designed and prepared. The microstructures were characterized by SEM, EBSD, EPMA, XRD, and TEM. The tensile mechanical properties at RT and cryogenic temperature (77 K) were investigated. Based on the experimental results, the conclusions are described as follows.

(1) After annealing at 675 °C for 60 min, a fully-recrystallized microstructure was formed for the V0 alloy. The grain size increased from 0.74 μm to 1.77 μm when the annealing temperature increased from 675 °C to 900 °C. Also, the grain sizes of other alloys increase with the increase of annealing temperatures. The XRD diffraction patterns of the fully-recrystallized alloys reveal a single phase.
(2) With the addition of V, the temperature of complete recrystallization increased gradually. The addition of V impedes the grain-boundary migration during the recrystallization and grain-growth processes.
(3) The 675 °C-annealed V0 alloy has a good combination of high YS (~1.3 GPa) and ductility (~13%) at RT. The increasing annealing temperature resulted in an increase in the EL and a decrease in the strength. The lattice-friction stress increased drastically with the addition of V. The large fluctuation of the atomic-bond distance is the predominant reason for the increase in the lattice-friction stress.
(4) The YS reached 1.8 GPa with 30% ductility for the 700 °C-annealed V0.5 alloy at 77 K, which is much higher than that at RT. After annealing at 800 °C, the V0.5 alloy exhibited an exceptional strength-ductility combination at 77 K. The YS is 1.4 GPa, UTS reached ~1.7 GPa, and the ductility was ~50%. The mechanical properties were superior to most of the reported HEAs and conventional alloys at cryogenic temperatures.
(5) The combination of dislocation, SF, and L-C lock results in a large strain-hardening rate and high strength during the tensile deformation at 77 K. The outstanding mechanical properties at 77 K were attributed to the recrystallized microstructure and the lattice-friction stress.

CRediT authorship contribution statement

Chengbin Wei: Conceptualization, Investigation, Methodology, Formal analysis, Writing – original draft, Validation. **Yiping Lu:** Writing – review & editing, Supervision, Funding acquisition. **Tongmin Wang:** Supervision, Funding acquisition. **Peter K. Liaw:** Writing – review & editing, Funding acquisition.

Declaration of competing interest

The authors declare that they have no known competing financial interests or personal relationships that could have appeared to influence the work reported in this paper.

Data availability

Data will be made available on request.

Acknowledgements

The present work was supported by the National Key Research and Development Program of China (Grant No. 2019YFA0209901 and 2018YFA0702901), the Liao Ning Revitalization Talents Program (XLYC1807047). P. K. L. very much appreciates the supports from (1) the National Science Foundation (DMR-1611180 and 1809640) with program directors, Drs. J. Yang, G. Shiflet, and D. Farkas and (2) the US Army Research Office (W911NF-13-1-0438 and W911NF-19-2-0049) with program managers, Drs. M.P. Bakas, S.N. Mathaudhu, and D.M. Stepp.

References

[1] B. Gludovatz, A. Hohenwarter, D. Catoor, E.H. Chang, E.P. George, R.O. Ritchie, A fracture-resistant high-entropy alloy for cryogenic applications, Science 345 (2014) 1153–1158.
[2] D. Li, C. Li, T. Feng, Y. Zhang, G. Sha, J.J. Lewandowski, P.K. Liaw, Y. Zhang, High-entropy Al0.3CoCrFeNi alloy fibers with high tensile strength and ductility at ambient and cryogenic temperatures, Acta Mater. 123 (2017) 285–294.
[3] T. Yang, Y.L. Zhao, W.P. Li, C.Y. Yu, J.H. Luan, D.Y. Lin, L. Fan, Z.B. Jiao, W.H. Liu, X.J. Liu, J.J. Kai, J.C. Huang, C.T. Liu, Ultrahigh-strength and ductile superlattice alloys with nanoscale disordered interfaces, Science 369 (2020) 427–432.
[4] Z. Lei, X. Liu, Y. Wu, H. Wang, S. Jiang, S. Wang, X. Hui, Y. Wu, B. Gault, P. Kontis, D. Raabe, L. Gu, Q. Zhang, H. Chen, H. Wang, J. Liu, K. An, Q. Zeng, T.G. Nieh, Z. Lu, Enhanced strength and ductility in a high-entropy alloy via ordered oxygen complexes, Nature 563 (2018) 546–550.
[5] D.B. Miracle, O.N. Senkov, A critical review of high entropy alloys and related concepts, Acta Mater. 122 (2017) 448–511.
[6] M.H. Chuang, M.H. Tsai, W.R. Wang, S.J. Lin, J.W. Yeh, Microstructure and wear behavior of AlxCo1.5CrFeNi1.5Tiyhigh-entropy alloys, Acta Mater. 59 (2011) 6308–6317.
[7] W. Li, D. Xie, D. Li, Y. Zhang, Y. Gao, P.K. Liaw, Mechanical behavior of high-entropy alloys, Prog. Mater. Sci. 118 (2021), 100777.
[8] B. Schuh, F. Mendez-Martin, B. Völker, E.P. George, H. Clemens, R. Pippan, A. Hohenwarter, Mechanical properties, microstructure and thermal stability of a nanocrystalline CoCrFeMnNi high-entropy alloy after severe plastic deformation, Acta Mater. 96 (2015) 258–268.
[9] Y. Zhang, T.T. Zuo, Z. Tang, M.C. Gao, K.A. Dahmen, P.K. Liaw, Z.P. Lu, Microstructures and properties of high-entropy alloys, Prog. Mater. Sci. 61 (2014) 1–93.
[10] F. Otto, A. Dlouhý, C. Somsen, H. Bei, G. Eggeler, E.P. George, The influences of temperature and microstructure on the tensile properties of a CoCrFeMnNi high-entropy alloy, Acta Mater. 61 (2013) 5743–5755.
[11] Z. Wu, H. Bei, G.M. Pharr, E.P. George, Temperature dependence of the mechanical properties of equiatomic solid solution alloys with face-centered cubic crystal structures, Acta Mater. 81 (2014) 428–441.
[12] J.Y. He, H. Wang, H.L. Huang, X.D. Xu, M.W. Chen, Y. Wu, X.J. Liu, T.G. Nieh, K. An, Z.P. Lu, A precipitation-hardened high-entropy alloy with outstanding tensile properties, Acta Mater. 102 (2016) 187–196.
[13] Y. Liang, L. Wang, Y. Wen, B. Cheng, Q. Wu, T. Cao, Q. Xiao, Y. Xue, G. Sha, Y. Wang, Y. Ren, X. Li, L. Wang, F. Wang, H. Cai, High-cohentent ductile coherent nanoprecipitated achieve ultrastrong high-entropy alloys, Nat. Commun. 9 (2018) 4063.
[14] M. Yang, D. Yan, F. Yuan, P. Jiang, E. Ma, X. Wu, Dynamically reinforced heterogeneous grain structure prolongs ductility in a medium-entropy alloy with gigapascal yield strength, Proc. Natl. Acad. Sci. U.S.A. 115 (2018) 7224–7229.
[15] X.H. Du, W.P. Li, H.T. Chang, T. Yang, G.S. Duan, B.L. Wu, J.C. Huang, F.R. Chen, C.T. Liu, W.S. Chuang, Y. Lu, M.L. Sui, E.W. Huang, Dual heterogeneous structures lead to ultrahigh strength and uniform ductility in a Co-Cr-Ni medium-entropy alloy, Nat. Commun. 11 (2020) 1–7.
[16] Y. Liu, Y. Cao, Q. Mao, H. Zhou, Y. Zhao, W. Jiang, Y. Liu, J.T. Wang, Z. You, Y. Zhu, Critical microstructures and defects in heterostructured materials and their effects on mechanical properties, Acta Mater. 189 (2020) 129–144.
[17] Y. Deng, C.C. Tasan, K.G. Pradeep, H. Springer, A. Kostka, D. Raabe, Design of a twinning-induced plasticity high entropy alloy, Acta Mater. 94 (2015) 124–133.
[18] Z. Li, F. Körmann, B. Grabowski, J. Neugebauer, D. Raabe, Ab initio assisted design of quinary dual-phase high-entropy alloys with transformation-induced plasticity, Acta Mater. 136 (2017) 262–270.
[19] M. Wang, Z. Li, D. Raabe, In-situ SEM observation of phase transformation and twinning mechanisms in an interstitial high-entropy alloy, Acta Mater. 147 (2018) 236–246.
[20] Z. Li, K.G. Pradeep, Y. Deng, D. Raabe, C.C. Tasan, Metastable high-entropy dual-phase alloys overcome the strength-ductility trade-off, Nature 534 (2016) 227–230.
[21] C. Lee, G. Song, M.C. Gao, R. Feng, P. Chen, J. Brechtl, Y. Chen, K. An, W. Guo, J. D. Poplawsky, S. Li, A.T. Samaei, W. Chen, A. Hu, H. Choo, P.K. Liaw, Lattice distortion in a strong and ductile refractory high-entropy alloy, Acta Mater. 160 (2018) 158–172.
[22] Y.F. Ye, Y.H. Zhang, Q.F. He, Y. Zhuang, S. Wang, S.Q. Shi, A. Hu, J. Fan, Y. Yang, Atomic-scale distorted lattice in chemically disordered equimolar complex alloys, Acta Mater. 150 (2018) 182–194.

[23] I. Toda-Caraballo, P.E.J. Rivera-Díaz-Del-Castillo, Modelling solid solution hardening in high entropy alloys, Acta Mater. 85 (2015) 14–23.

[24] S.S. Sohn, A. Kwiatkowski da Silva, Y. Ikeda, F. Körmann, W. Lu, W.S. Choi, B. Gault, D. Ponge, J. Neugebauer, D. Raabe, Ultrastrong medium-entropy single-phase alloys designed via severe lattice distortion, Adv. Mater. 31 (2019), 1807142.

[25] R. Chang, W. Fang, X. Bai, C. Xia, X. Zhang, H. Yu, B. Liu, F. Yin, Effects of tungsten additions on the microstructure and mechanical properties of CoCrNi medium entropy alloys, J. Alloys Compd. 790 (2019) 732–743.

[26] W. Lu, C.H. Liebscher, G. Dehm, D. Raabe, Z. Li, Bidirectional transformation enables hierarchical nanolaminate dual-phase high-entropy alloys, Adv. Mater. 30 (2018) 1–10.

[27] M. Komarasamy, S. Shukla, N. Ley, K. Liu, K. Cho, B. McWilliams, R. Brennan, M. L. Young, R.S. Mishra, A novel method to enhance CSL fraction, tensile properties and work hardening in complex concentrated alloys – Lattice distortion effect, Mater. Sci. Eng. 736 (2018) 383–391.

[28] A.J. Zaddach, C. Niu, C.C. Koch, D.L. Irving, Mechanical properties and stacking fault energies of NiFeCrCoMn high-entropy alloy, JOM 65 (2013) 1780–1789.

[29] R.K. Ray, Rolling textures of pure nickel, nickel-iron and nickel-cobalt alloys, Acta Metall. Mater. 43 (1995) 3861–3872.

[30] D.M. Symons, Hydrogen embrittlement of Ni-Cr-Fe alloys, Metall. Mater. Trans. A A 28 (1997) 655–663.

[31] P.C.J. Gallagher, The influence of alloying, temperature, and related effects on the stacking fault energy, Met. Trans. 1 (1970) 2429–2461.

[32] M.P. Agustianingrum, S. Yoshida, N. Tsuji, N. Park, Effect of aluminum addition on solid solution strengthening in CoCrNi medium-entropy alloy, J. Alloys Compd. 781 (2019) 866–872.

[33] X.L. Huang, L.P. Huang, H.L. Peng, Y. Liu, B. Liu, S. Li, Enhancing strength-ductility synergy in a casting non-equiatomic NiCoCr-based high-entropy alloy by Al and Ti combination addition, Scripta Mater. 200 (2021), 113898.

[34] S.G. Ma, Y. Zhang, Effect of Nb addition on the microstructure and properties of AlCoCrFeNi high-entropy alloy, Mater. Sci. Eng., A 532 (2012) 480–486.

[35] W.H. Liu, Z.P. Lu, J.Y. He, J.H. Luan, Z.J. Wang, B. Liu, Y. Liu, M.W. Chen, C.T. Liu, Ductile CoCrFeNiMox high entropy alloys strengthened by hard intermetallic phases, Acta Mater. 116 (2016) 332–342.

[36] X. Huang, N. Hansen, N. Tsuji, Hardening by annealing and softening by deformation in nanostructured metals, Science 312 (2006) 249–251.

[37] X.Y. Zhang, Q. Liu, X.L. Wu, A.W. Zhu, Work softening and annealing hardening of deformed nanocrystalline nickel, Appl. Phys. Lett. 93 (2008) 1–4.

[38] S. Praveen, J. Wung, P. Asghari-rad, J. Min, H. Seop, Annealing-induced hardening in high-pressure torsion processed CoCrNi medium entropy alloy, Mater. Sci. Eng. 734 (2018) 338–340.

[39] J. Gu, M. Song, Annealing-induced abnormal hardening in a cold rolled CrMnFeCoNi high entropy alloy, Scripta Mater. 162 (2019) 345–349.

[40] G. Laplanche, A. Kostka, O.M. Horst, G. Eggeler, E.P. George, Microstructure evolution and critical stress for twinning in the CrMnFeCoNi high-entropy alloy, Acta Mater. 118 (2016) 152–163.

[41] S.J. Sun, Y.Z. Tian, H.R. Lin, Z.J. Wang, Z.F. Zhang, Revisiting the role of prestrain history in the mechanical properties of ultrafine-grained CoCrFeMnNi high-entropy alloy, Mater. Sci. Eng. 801 (2021), 140398.

[42] Y.H. Jo, S. Jung, W.M. Choi, S.S. Sohn, H.S. Kim, B.J. Lee, N.J. Kim, S. Lee, Cryogenic strength improvement by utilizing room-temperature deformation twinning in a partially recrystallized VCrMnFeCoNi high-entropy alloy, Nat. Commun. 8 (2017), 15719.

[43] L.B. Chen, R. Wei, K. Tang, J. Zhang, F. Jiang, J. Sun, Ductile-brittle transition of carbon alloyed Fe40Mn40Co10Cr10 high entropy alloys, Mater. Lett. 236 (2019) 416–419.

[44] B. Gludovatz, A. Hohenwarter, K.V.S. Thurston, H. Bei, Z. Wu, E.P. George, R. O. Ritchie, Exceptional damage-tolerance of a medium-entropy alloy CrCoNi at cryogenic temperatures, Nat. Commun. 7 (2016), 10602.

[45] Z. Wu, H. Bei, Microstructures and mechanical properties of compositionally complex Co-free FeNiMnCr-18 FCC solid solution alloy, Mater. Sci. Eng. 640 (2015) 217–224.

[46] Y. Tong, D. Chen, B. Han, J. Wang, R. Feng, T. Yang, C. Zhao, Y.L. Zhao, W. Guo, Y. Shimizu, C.T. Liu, P.K. Liaw, K. Inoue, Y. Nagai, A. Hu, J.J. Kai, Outstanding tensile properties of a precipitation-strengthened FeCoNiCrTi0.2 high-entropy alloy at room and cryogenic temperatures, Acta Mater. 165 (2019) 228–240.

[47] G. Laplanche, A. Kostka, C. Reinhart, J. Hunfeld, G. Eggeler, E.P. George, Reasons for the superior mechanical properties of medium-entropy CrCoNi compared to high-entropy CrMnFeCoNi, Acta Mater. 128 (2017) 292–303.

[48] J. Miao, C.E. Slone, T.M. Smith, C. Niu, H. Bei, M. Ghazisaeidi, G.M. Pharr, M. J. Mills, The evolution of the deformation substructure in a Ni-Co-Cr equiatomic solid solution alloy, Acta Mater. 132 (2017) 35–48.

[49] T. Bhattacharjee, R. Zheng, Y. Chong, S. Sheikh, S. Guo, I.T. Clark, T. Okawa, I. S. Wani, P.P. Bhattacharjee, A. Shibata, N. Tsuji, Effect of low temperature on tensile properties of AlCoCrFeNi2.1 eutectic high entropy alloy, Mater. Chem. Phys. 210 (2018) 207–212.

[50] C. Zheng, W. Yu, Effect of low-temperature on mechanical behavior for an AISI 304 austenitic stainless steel, Mater. Sci. Eng. 710 (2018) 359–365.

[51] S.S. Sohn, S. Hong, J. Lee, B.C. Suh, S.K. Kim, B.J. Lee, N.J. Kim, S. Lee, Effects of Mn and Al contents on cryogenic-temperature tensile and Charpy impact properties in four austenitic high-Mn steels, Acta Mater. 100 (2015) 39–52.

[52] W.H. Liu, Y. Wu, J.Y. He, T.G. Nieh, Z.P. Lu, Grain growth and the Hall-Petch relationship in a high-entropy FeCrNiCoMn alloy, Scripta Mater. 68 (2013) 526–529.

[53] J. Bok, J. Wung, Z. Li, J. Chan, J. Gi, D. Raabe, H. Seop, Boron doped ultrastrong and ductile high-entropy alloys, Acta Mater. 151 (2018) 366–376.

[54] H. Adrian, F.B. Pickering, Effect of titanium additions on austenite grain growth kinetics of medium carbon V-Nb steels containing 0.008-0.018%N, Mater. Sci. and Tech-Lond. 7 (1991) 176–182.

[55] H.V. Atkinson, Theories of normal grain growth in pure single phase systems, Acta Metall. 36 (1988) 469–491.

[56] J.E. Burke, D. Turnbull, Recrystallization and grain growth, Prog. Met. Phys. 3 (1952) 220–244.

[57] F.J. Humphreys, M. Hatherly, Recrystallization and Related Annealing Phenomena, second ed., Elsevier Ltd, 2004.

[58] S. Yoshida, T. Ikeuchi, T. Bhattacharjee, Y. Bai, A. Shibata, N. Tsuji, Effect of elemental combination on friction stress and Hall-Petch relationship in face-centered cubic high/medium entropy alloys, Acta Mater. 171 (2019) 201–215.

[59] H.S. Oh, K. Odbadrakh, Y. Ikeda, S. Mu, F. Körmann, C.J. Sun, H.S. Ahn, K.N. Yoon, D. Ma, C.C. Tasan, T. Egami, E.S. Park, Element-resolved local lattice distortion in complex concentrated alloys: an observable signature of electronic effects, Acta Mater. 216 (2021), 117135.

[60] Z.C. Cordero, B.E. Knight, C.A. Schuh, Six decades of the Hall–Petch effect – a survey of grain-size strengthening studies on pure metals, Int. Mater. Rev. 61 (2016) 495–512.

[61] A. Haglund, M. Koehler, D. Catoor, E.P. George, V. Keppens, Polycrystalline elastic moduli of a high-entropy alloy at cryogenic temperatures, Intermetallics 58 (2015) 62–64.

[62] C. Varvenne, G.P.M. Leyson, M. Ghazisaeidi, W.A. Curtin, Solute strengthening in random alloys, Acta Mater. 124 (2017) 660–683.

[63] C. Varvenne, A. Luque, W.A. Curtin, Theory of strengthening in fcc high entropy alloys, Acta Mater. 118 (2016) 164–176.

[64] L. Fan, T. Yang, Y. Zhao, J. Luan, G. Zhou, H. Wang, Z. Jiao, C.T. Liu, Ultrahigh strength and ductility in newly developed materials with coherent nanolamellar architectures, Nat. Commun. 11 (2020) 1–8.

[65] J.P. Hirth, J. Lothe, Theory of Dislocations, second ed., J. Appl. Mech. Wiley, New York, 1983, pp. 306–353, 50.

[66] X.L. Wu, Y.T. Zhu, Y.G. Wei, Q. Wei, Strong strain hardening in nanocrystalline nickel, Phys. Rev. Lett. 103 (2009) 1–4.

[67] S. Chen, H.S. Oh, B. Gludovatz, S.J. Kim, E.S. Park, Z. Zhang, R.O. Ritchie, Q. Yu, Real-time observations of TRIP-induced ultrahigh strain hardening in a dual-phase CrMnFeCoNi high-entropy alloy, Nat. Commun. 11 (2020) 1–8.